Schweizerische Eidgenossenschaft
Confédération suisse
Confederazione Svizzera
Confederaziun svizra

Department of the Environment,
Transport, Energy and Communication DETEC

Swiss Federal Office of Energy SFOE
Energy Research and Cleantech

Final report

INTENT

Interface engineering of perovskite/silicon tandem solar cells for improved performance and stability

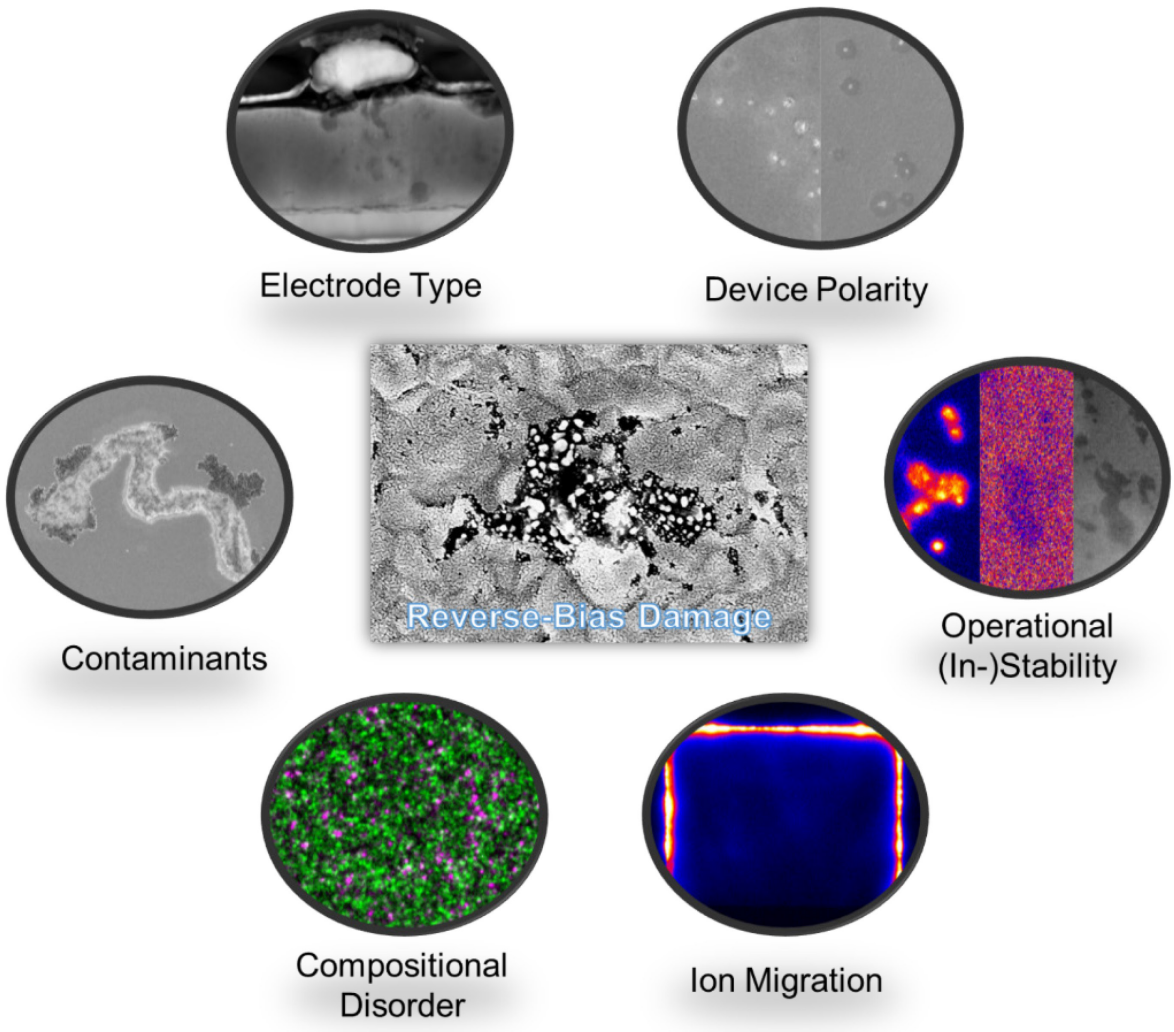

Date: December 2021

Place: Neuchâtel

Publisher:
Swiss Federal Office of Energy SFOE
Programme Photovoltaics
CH-3003 Bern
www.bfe.admin.ch

Financed by:
Swiss Federal Office of Energy SFOE
Programme Photovoltaics
CH-3003 Bern
www.bfe.admin.ch

Authors:
Daniel Jacobs, EPFL-PVLAB, daniel.jacobs@epfl.ch
Quentin Jeangros, EPFL-PVLAB, quentin.jeangros@epfl.ch
Christophe Ballif, EPFL-PVLAB, christophe.ballif@epfl.ch

SFOE Head of domain: Stefan Oberholzer, stefan.oberholzer@bfe.admin.ch
SFOE Programme manager: Stefan Oberholzer, stefan.oberholzer@bfe.admin.ch
SFOE Contract number: SI/501804-01

Summary

Perovskite/silicon tandems have been identified as a promising candidates to overcome the efficiency limitations of single-junction solar cells at low production cost. However, state-of-the-art perovskite-based solar cells have so far failed to survive the reverse bias conditions that may occur when a module is partially shaded in the field. The aim of this project was to clarify the mechanisms controlling this degradation and to develop optimized tandem cell architectures with greater resilience to partial-shading conditions.This report summarises the scientific outcomes of INTENT, which will be the subject of at least two publications currently under revision, and details the progress made towards improving the reverse-bias stability of perovskite/silicon tandems.

Résumé

Les cellules tandems pérovskite/silicium ont été identifiées comme des candidats prometteurs pour surmonter les limites d'efficacité des cellules solaires à simple jonction à un faible coût de production. Cependant, les cellules solaires de pointe à base de pérovskite n'ont pas réussi jusqu'à présent à survivre aux conditions de polarisation inverse qui peuvent se produire lorsqu'un module est partiellement ombragé sur le terrain. Ce rapport résume les résultats scientifiques d'INTENT, qui feront l'objet d'au moins deux publications actuellement en cours de révision, et détaille les progrès réalisés dans l'amélioration de la stabilité du polarisation inverse des tandems pérovskite/silicium.

Zusammenfassung

Perowskit-Silicium-Tandem-Solarzellen haben sich als vielversprechende Kandidaten erwiesen, um die Effizienzbeschränkungen von Solarzellen mit nur einem Übergang bei niedrigen Produktionskosten zu überwinden. Moderne Solarzellen auf Perowskit-Basis haben jedoch bisher die Bedingungen der Sperrspannung nicht überstanden, die auftreten können, wenn ein Modul im Feld teilweise verschattet ist. Dieser Bericht fasst die wissenschaftlichen Ergebnisse von INTENT zusammen, die Gegenstand von mindestens zwei Veröffentlichungen sein werden, die derzeit überarbeitet werden, und beschreibt die Fortschritte, die bei der Verbesserung der Stabilität von Perowskit-Silizium-Tandems in Sperrrichtung erzielt wurden.

List of abbreviations

WP	Work package
RB	Reverse bias
TCO	Transparent conductive oxide
SAM	Self-assembled monolayer
HTL	Hole-transport layer
SEM	Scanning Electron Microscopy
TEM (EDX)	Transmission Electron Microscopy (Energy-Dispersive X-ray Spectroscopy)
Bottom, Top	With respect to a solar cell: the first and last layers (respectively) in order of fabrication
Front, Rear	With respect to a solar cell: the sky- and ground-facing surfaces (respectively).
PL	Photoluminescence
EL	Electroluminescence
SIMS	Secondary Ion Mass Spectrometry

Contents

1 Flat and textured single-junctions and tandems (Work-package 1)

To ensure the greatest relevance for our subsequent work (developing mechanistic understanding and more resilient architectures), work-package 1 was designed to establish processes for fabricating a selection of high-efficiency cell types, including devices on textured substrates emulating the surface of industrial Si bottom-cells.

M1 - Identification of the most promising strategy to fabricate textured substrates for perovskite single junctions (ZnO, inactive textured Si wafer or replicate of the Si texture).

D1 – Comparison of J-V curves of single-junction perovskite solar cells made on different textures, with one cell design achieving a Voc >1.15 V for a Eg of 1.7 eV (for an active area >1 cm^2).

Several methods were investigated with the aim of fabricating perovskite single-junctions on different textures. In particular, devices were made on natively textured ZnO, inactive textured Si wafers, and polymer replicas of Si textures, as originally described in the proposal. Inactive Si wafers (identical to fully functional tandems from the perspective of the perovskite top cell) were found to yield the best performance and the greatest reliability in terms of avoiding particle contamination.

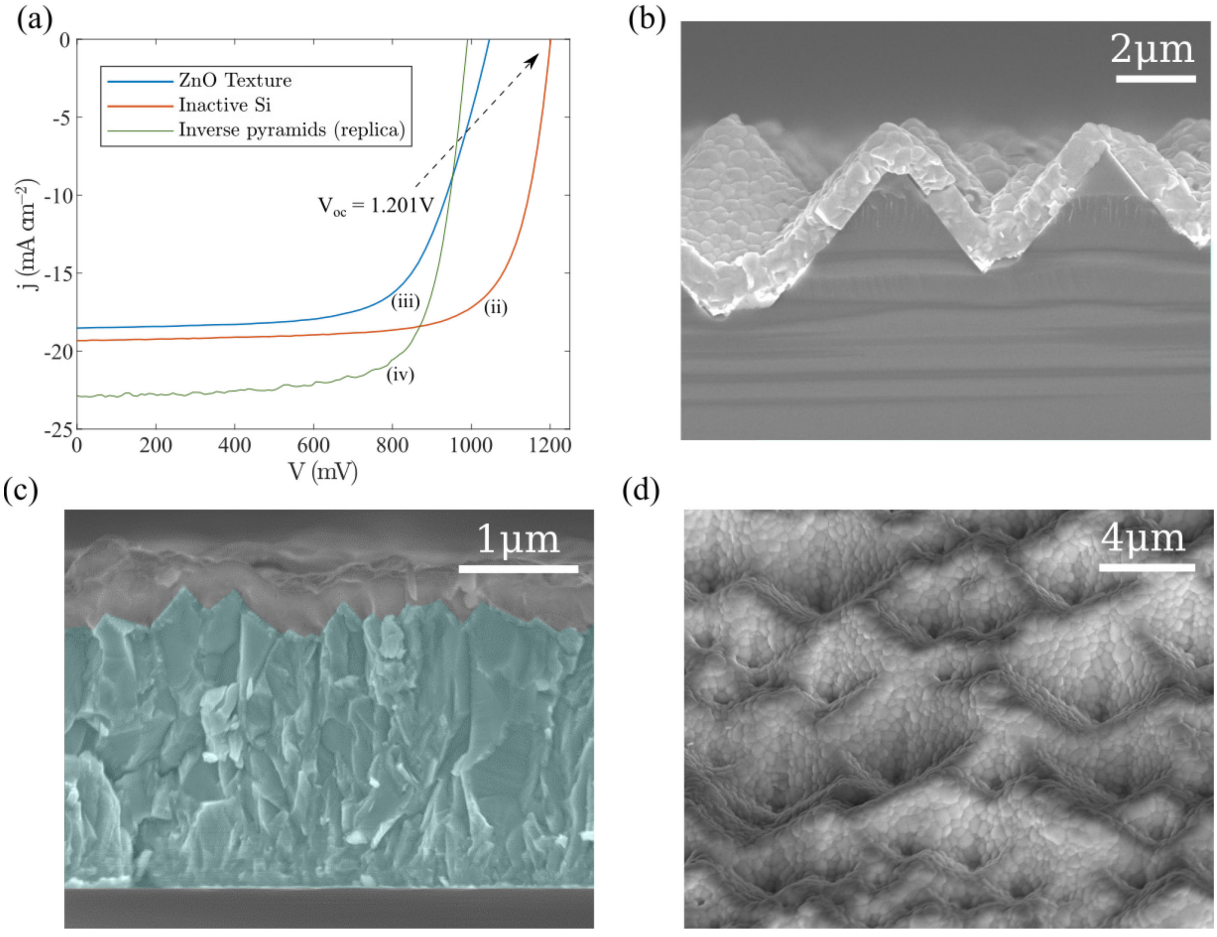

Figure 1: (a) J-V curves of single-junction perovskite cells made on different textures. The device made on inactive Si with V_{oc}= 1.201V had an active area of 1.42cm^2. The device on the inverse-pyramid texture was made with a lower bandgap perovskite, accounting for the higher current values. (b-d) SEM micrographs of the different cell types: (b) cross-section showing a perovskite film on inactive Si, (c) cross-section of a perovskite cell on ZnO, with the substrate highlighted in colour, (d) top-view of a perovskite film on a partially replicated texture: an imprint of the random pyramid Si texture was taken in UV-curable lacquer to yield 'inverse pyramids' for this sample (others samples were made on fully replicated textures).

A comparison of I-V performance is shown in Fig. 1 alongside SEM micrographs of each structure. Notably, the D1 goal of V_{oc} > 1.15V was achieved with a bandgap of only 1.67eV, instead of 1.7eV.

M2 - Selection of >3 perovskite cell architectures (inorganic and organic carrier-selective contacts, amorphous and transparent TCOs and potentially different perovskite fabrication route) for high efficiency single-junction and tandem fabrication.

D2 - J-V curves of 3 perovskite/silicon tandem cell designs showing an efficiency potential >26% at maximum power point on >1cm2, with at least one tandem design demonstrating this efficiency value.

To ascertain the impact of contact layers, TCOs, and the perovskite absorber itself on reverse-bias stability, devices were made (and in some cases acquired from collaborators) with many variations on our 'baseline' cell-structure. For the majority of experiments we confined attention to p-i-n devices, as these are of great interest for straightforward tandem integration. For comparison, a few devices with opposite polarity (n-i-p instead of p-i-n) were also tested for their stability in reverse bias, having either the structure ITO-glass/C_{60}/CsFA Perovskite/Spiro-OMeTAD/Au (fabricated at PVLab), or ITO-glass/TiO_2/CsFA Perovskite/Spiro-OMeTAD/Au (supplied by collaborators).

The variations conducted on our baseline p-i-n process are summarized in the table below, grouped by layer:

Substrate	glass/ITO, inactive Si+ITO, inactive Si+nuc/puc recombination junction
Hole transport layer	NiO_x, Spiro-TTB, TaTm, self assembled monolayers (MeO-2PaCz, Me-4PaCz)
Absorber	$Cs_yFA_{1-y}PbI_{3-x}Br_x$ (hybrid method), $Cs_yFA_{1-y}PbI_{3-x}Br_x$ (one-step method), $Cs_yMA_zFA_{1-y-z}PbI_{3-x}Br_x$ (one-step method)
Electron transport layer	neat C_{60}, LiF+C_{60}, C_{60} + SnO_x (of varying thickness), neat SnO_x, PCBM
Top Electrode	Metal-only: Ag, Ag+TmPyBP, Cu + BCP, Au, Pb, Carbon paste TCO+metal: IZO+Ag, IZO+Cu, IZO+Ni/Al, IZO+Al, ITO+Ag, IZrO + Ag. TCO-only: IZO

We note that several of the above were investigated purely for the sake of probing mechanisms of reverse-bias failure and did not yield viable solar cells in terms of photovoltaic performance (e.g. p-i-n devices with Pb or Au full-area electrodes).

A number of cell architectures with layers in the table above were found to yield device efficiencies over 26% when incorporated into fully textured Si-perovskite tandems. We summarize a selection of these results in Fig. 2.

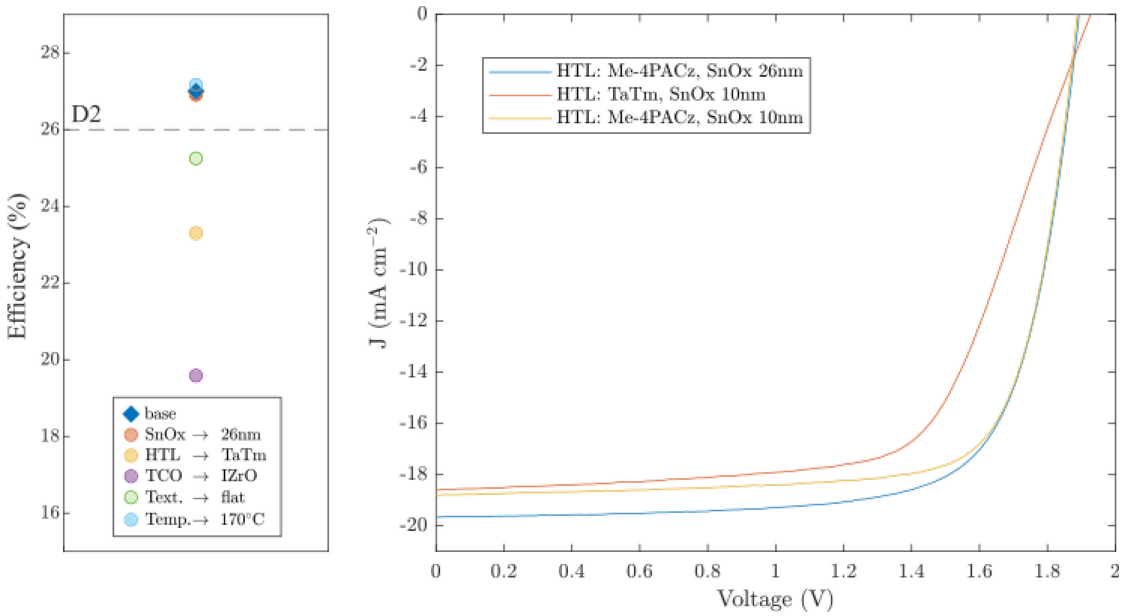

Figure 2: Tandem device efficiencies and J-V curves showcasing a small selection the of devices fabricated in WP1. All pictured devices featured active areas >1cm^2. The designation 'base' on the left refers to a top-cell stack /ITO/Me-4PACz/Perovskite/C_{60}/SnOx(10nm)/IZO/Ag on a fully textured Si bottom-cell, which constitutes the lab's baseline process for tandem fabrication at the time of writing. Substitutions relative to this sequence are indicated in the legends.

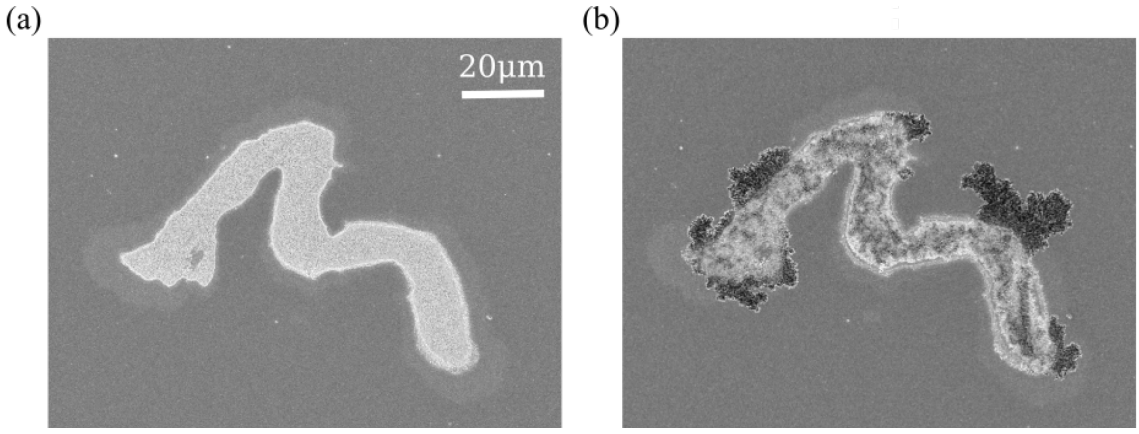

Figure 3: Detrimental effect of particle contamination on reverse-bias stability. (a,b) SEM micrographs of an unidentified contaminant inside the active area of a single-junction cell, shown before (a) and after (b) the application of reverse bias. Degradation can be seen spreading from the contaminant into the surrounding area.

2 Identification of the mechanisms controlling reverse bias failure (Work-package 2)

Work-package 2 dealt mostly with establishing a mechanistic understanding of reverse-bias failure, beginning with basic reverse-stability tests on the devices of Work-package 1, before moving to more in-depth characterization of a few select architectures. The main scientific outcomes of these studies will be summarized briefly below, with further details to be provided in forthcoming publications.

M3 - Identification of the role of perovskite crystallinity and optoelectronic quality, choice of carrier-selective contacts and electrodes, substrate texture, temperature, illumination spectrum and intensity on the reverse bias degradation of perovskite single junctions and tandem solar cells.

Device quality: shunting due to particle contamination

An early but crucial outcome of this study was the observation that reverse-stability is highly sensitive to particle contamination, to a much greater degree than cell efficiency. Particles inside the active area, though frequently benign under forward bias, are often found to transform into hotspots or shunts following RB exposure in a manner that is highly detrimental to subsequent device performance.

The sensitivity to contamination is such that investigating the role of intrinsic factors, such as perovskite crystallinity, the choice of contacts, and substrate texturing, proved extremely challenging before this issue was properly identified. Reverse-bias behaviour in electrical measurements can be altered drastically by the presence of a single microscopic particle measuring a few square microns or less within active areas up to square centimetres in size. The observation that particle contamination can be “invisible” in terms of cell performance but completely undermine a cell’s RB stability is significant in terms of implications for large-scale manufacturing and testing.

Several early experiments, aimed at comparing the role of contact materials and texturing, were compromised by the pervasiveness of particle contamination. These observations prompted a lab-wide

effort to combat the issue, a process which ongoing and has led to noticeable increases in batch yield and consistency across several perovskite activities, as well as improvements in RB stability.

Perovskite quality: role of stoichiometry and quality (including aging)

One critical aspect of perovskite quality for all photovoltaic metrics, from efficiency to stability, is the stoichiometry of the compound, i.e. the ratio of its components. With respect to perovskites denoted as ABX_3, stoichiometry generally refers to the ratio of AX to BX_2 (the two main precursors in both hybrid and one-step perovskite preparation). A film with an insufficient or excess amount of AX will be referred to as “under-“ and “over-converted” respectively, in allusion to two-step processes where a film of mostly BX_2 is converted to perovskite through the addition of AX. Microscopically, deviations from ideal stoichiometry will be reflected in the presence of vacancies, interstitial atoms, or un-reacted precursor within the perovskite film and/or its surfaces.

Both under- and over-conversion were found to have significant effects on RB degradation, highlighting the need for precise stoichiometric control. Under-converted films (those with excess PbI_2) were found to harbour a higher concentration of voids on their bottom surfaces than control films following reverse-bias stress, suggesting a greater degree of mass loss as a result of RB (Fig. 4a). Excess PbI_2 is already well-known to compromise stability under operational conditions – these observations suggest that its presence compromises reverse-stability as well. An interesting supplementary observation concerning the voids appearing in Fig 4a is that these also be observed in films that have simply been aged in storage, indicating that the process of RB decomposition is connected with other aspects of perovskite instability.

Over-conversion on the other hand enhances the micron-scale inhomogeneity that is visible in photoluminescence (PL) maps as seen in Fig. 4b:i. These photo-luminescent domains are correlated with the location of localized electro-luminescence (EL) that can be detected during RB-stressing, as shown in Fig. 4b:ii. Electroluminescence under reverse-bias is an unexpected observation in itself, since simultaneous injection of both electrons and holes is needed to produce a luminescent recombination event. The correlation of RB-EL spots with the domains identified in PL suggests that non-uniform carrier injection under RB is primarily related to properties of the perovskite itself (e.g. local stoichiometry), rather than to characteristics of the contact layers (e.g. variations in thickness). The luminescent

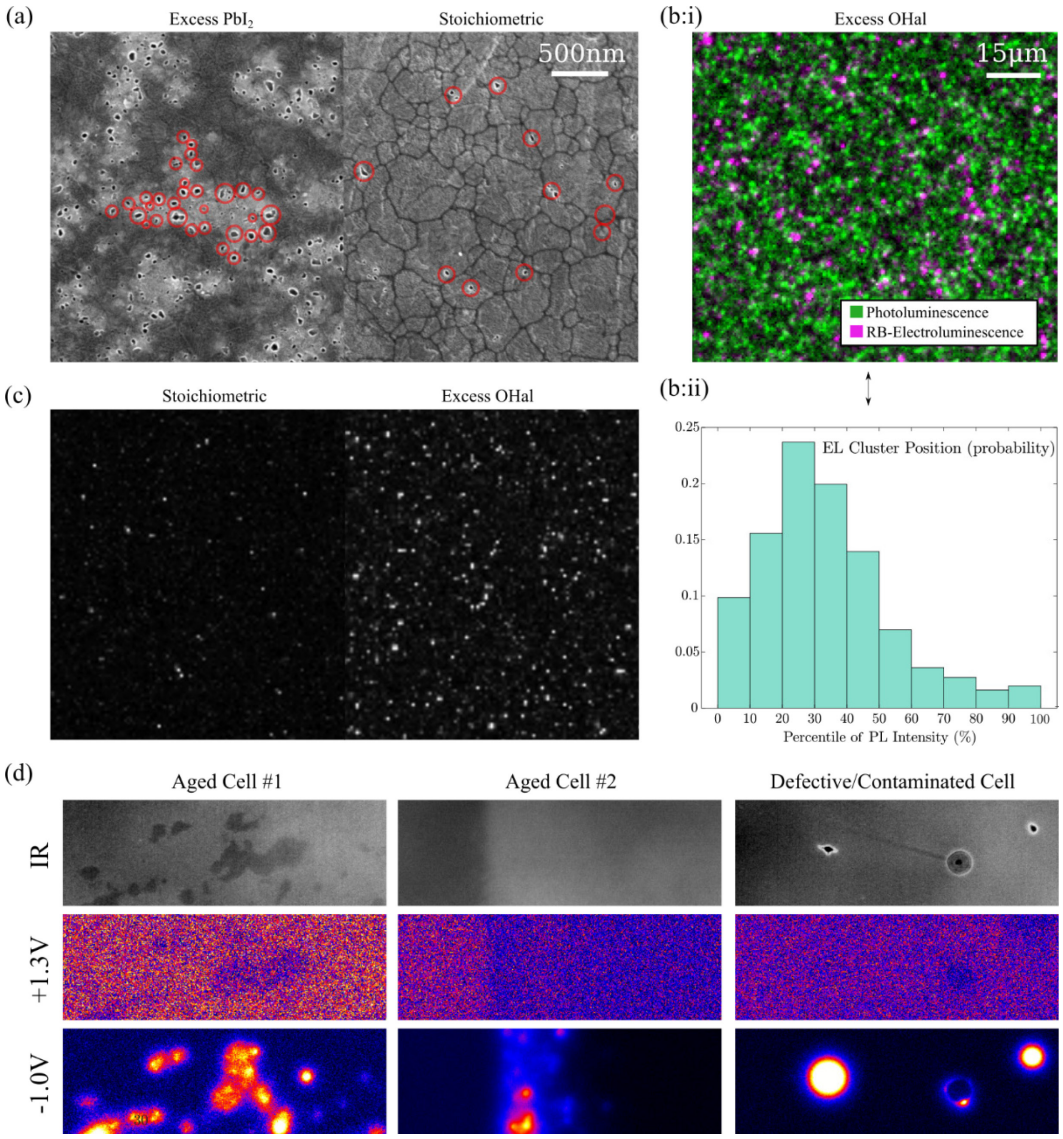

Figure 4: Effect of perovskite characteristics on reverse-bias degradation and different manifestations of degradation. (a) SEM micrograph showing the bottom surface of two perovskite films peeled from their substrate after reverse-biasing (-4V, 30s). Damage is visible in the form of voids on the bottom surface (and possibly elsewhere in the film), highlighted in red. The image contrasts a film that was deliberately made using an excess of PbI_2 (left), with a stoichiometric film (right). Voids are notably concentrated on the boundaries of PbI_2-rich domains (left, bright regions). (b:i) Composite image of photoluminescence intensity (green, taken under ~1-sun LED illumination before biasing), and reverse-bias electroluminescence (purple, -4V), acquired in the active area of a single-junction cell on ITO/glass. (b:ii) Histogram showing the correlation between photoluminescence and RB-EL: more than 50% of the EL intensity is found clustered in regions lying between the 10^{th} and 40^{th} percentile of PL intensity. (c) Luminescence images acquired at approximately equal current density showing a higher density of luminescent clusters in the device with excess organohalide (OHal). (d) Infrared images (top row) and lock-in thermography maps (middle and bottom rows) of two different cells (left, right) tested after aging for 3 weeks in storage. Regions of differing contrast in the IR image indicate the beginnings of a degradation process which makes the cell more vulnerable to reverse-bias degradation, as seen in the -1.0V image.

domains in these measurements can be correlated with compositional variations, in particular of the organo-halide component, as measured by nano-SIMS (data not shown).

Observations of RB-induced electroluminescence (Figs. 4b:I and 4c) show that our baseline p-i-n cells pass reverse current via the injection of both electrons and holes, at least in some isolated locations. Notably, the size and distribution of these luminescent spots matches patterns of hotspot-damage seen

in top-view SEM (e.g. Fig 8 below). Perovskite stoichiometry seems to play a role in determining the balance of electron versus hole injection: as shown in Fig 4(d:ii), films with an excess of the organo-halide component were seen to luminesce more strongly than stoichiometric films, despite passing nearly equal current densities (data not shown). Although this does not suggest an immediate remedial strategy for reverse-stability, it underscores sensitivity of reverse-bias characteristics to film stoichiometry as discussed above in reference to under-converted films.

Remaining on the topic of perovskite quality, we also observed significant interactions between "operational" degradation (i.e. that induced by any combination of light, forward bias, or unbiased time in darkness) and RB degradation, which is relevant to the long-term RB stability of perovskite solar cells. For example, devices left to age in storage for a period of several weeks before RB showed some discolouration in their active area visible with an infrared camera (Fig 4c). The initial application of forward bias did not reveal these discoloured regions as active for current injection, implying that the process causing this degradation does little to harm the cell's efficiency. Nonetheless, such regions were found to pass a much higher reverse current density than the surrounding active area. This indicates that resilience to RB-stressing can be expected to decrease as a cell ages, and underscores the role of the perovskite's quality and integrity in dictating RB stability. The correlation could be a result of mobile ion release during perovskite decomposition, a high concentration of which is known to facilitate reverse current injection. [1]

Role of selective contacts & ALD Buffer

Contact layers, principally the ETL and HTL, have vital roles to play in terms of RB characteristics. As long as all cell layers remain intact, reverse current can only pass through an un-illuminated solar cell via tunnelling, which entails a strong sensitivity to internal electric fields and hence the contact dielectric properties (capacitance). The expected dependency follows from elementary considerations: at a given applied potential, internal fields will be weaker in cells with thicker contact layers, and tunnelling currents should be correspondingly smaller. This trend was verified in several experiments focusing on the ETL contact, which is expected to be the "limiting" contact for tunnelling, being the one with a lower capacitance in our baseline process (C_{60} having a relatively small dielectric constant and large thickness compared to typical HTL layers). In Fig 5a we show results from an experiment in which the evaporated C_{60} layer in our baseline process was substituted for a spin-coated PCBM layer of greater thickness. During RB stress-testing, the cells with the thicker PCBM layers passed significantly less reverse current, and retained more of their initial photovoltaic efficiency. In another similar experiment shown in Fig 5b, the thickness of our baseline C_{60} layer was co-varied with the thickness of SnO_x (the buffer layer above C_{60}) and similar trends emerged: namely, reverse-current decreased considerably with the thickness of top ETL stack (ETL+buffer layer). For cells under the protection of a bypass diode, this represents a viable strategy to increasing reverse-bias tolerance, since preventing current flow altogether avoids the issues caused by inhomogeneous injection (e.g. Fig 5d:ii), which appears to be tied to hotspot formation. In the absence of a bypass diode the strategy of using thicker contact layers may be inadequate since resilience under a current of $-J_{MPP}$ is necessary.

Concerning the HTL, similar experiments were performed with less conclusive results. Tests with the small-molecule TaTm as HTL (not shown) were compromised on several occasions by particle contamination as discussed above, likely due to its deposition in a chamber also used for metal evaporation. We also compared cells made with SAM HTLs where the SAM was either deposited directly on ITO or on the inorganic HTL NiOx. In Fig 5c we show measurements of reverse current in these devices which exhibit the expected trend going from a bare SAM (MeO-2PACz) to SAM+NiOx, namely, reduced reverse current as anticipated from a reduced capacitance in the presence of NiOx. However, an unexpected increase in reverse current relative to both was seen in the case of bare NiOx. Despite these apparent trends, the noise in these latter current measurements (generally indicative of localized

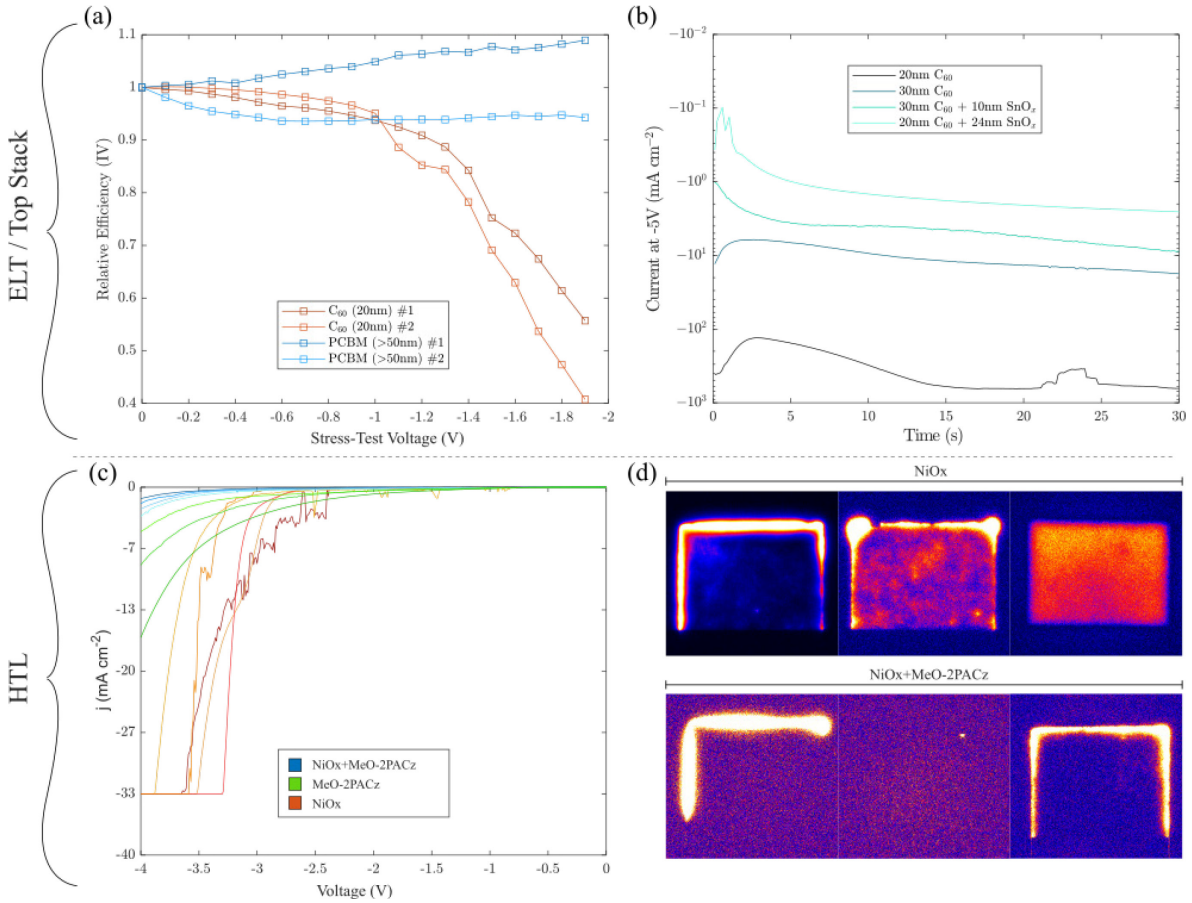

Figure 5: Effect of contact-layer characteristics on reverse-bias degradation. Increasing the thickness of the top-stack (ETL+SnOx buffer layer) was found to significantly supress reverse current injection and RB damage, even for layers such as C_{60} that are ineffective as barriers. (a) Data showing the evolution of relative efficiency during a reverse-bias stress-test in which the cells were biased at successively lower voltages with IV-measurements after each step. (b) Current measurements at -5V showing that thicker top-electrode stacks are effective in suppressing reverse current. (c) J-V sweeps comparing devices made on different HTL layers. These tests were compromised by the appearance of point-shunting in the NiOx curves (evident in the noisy signal), and inhomogeneous current flow as seen in lock-ion thermography measurements of the same devices (d).

breakdown) and the information provided by lock-in thermography shown in Fig 5(iv) demonstrates that not all cells in this experiment were passing reverse-current homogeneously, with several showing a preference for reverse-current injection along active-area boundaries. These observations precipitated the insights that will be discussed below in reference to D4 (“Edge breakdown and lateral ion migration”).

To conclude our summary of contact-layer effects on reverse-breakdown, we confirmed expected trends with respect to the top contact (ETL for our p-i-n devices), namely that increased thickness tends to supress reverse-current injection. The bottom contact (HTL) on the other hand has an influence which is less clear. This may be justified by our observation that perovskite crystal quality has a strong effect on RB behaviour, and the fact that the bottom contact is known to have a strong influence on perovskite formation and crystallization. Differences in grain size for example are evident when comparing hybrid perovskites prepared on ITO/SAM substrates versus bare ITO or bare glass (data not shown).

Role of electrode

Early observations of reverse-bias failure in semi-transparent devices (those with a full-area TCO electrode and partial-area metallization) indicated that the presence of a metal electrode increases vulnerability to RB-induced shunt formation. Localized current injection and hotspots were seen to occur in the non-metallized regions of semi-transparent cells, as well as in those with TCO-only electrodes (Figure 8a,b), but with apparently lower frequency in the latter. Since RB-induced shunt formation is not exclusive to devices with metal electrodes, we regard the process as unlikely to be associated with

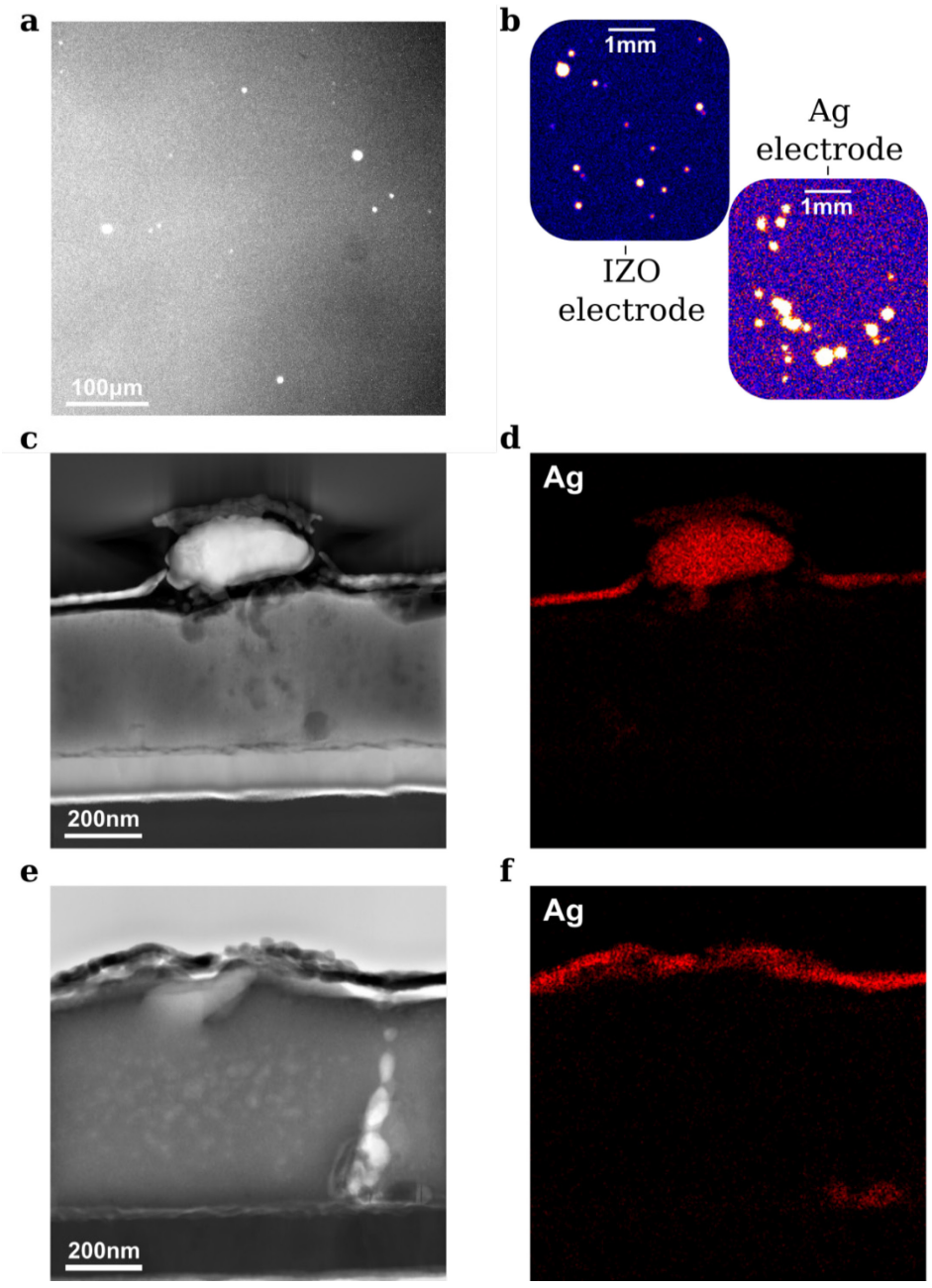

Figure 6: (a) Luminescence image of an un-metallized (TCO-only) active area subject to -7V, showing localized carrier injection (similar to the images shown in Fig 5d:ii for metal electrodes). (b) Heat maps acquired with lock-in thermography showing hotspot formation in both metallized and un-metallized cells as a result of RB-stressing (these hotspots were not present in initial forward-bias measurements). (c,e) TEM micrographs showing cross-sectional views of a thin-electrode (Ag) cell that was subjected to RB stress at -4V for 30s. Blobs on the top surface correspond to dissolved Ag as seen in (d) (TEM EDX). (f) Metal can also be detected within the bulk of the perovskite film.

metal-filament formation, as suggested in some publications on perovskite memory devices. Instead, the increased vulnerability of metallized regions to shunt formation may be a simple result of their lower sheet resistance (typical top-stack TCO layers contributing around 80Ohm, and metal layers less than 0.1Ohm), allowing for larger localized current densities and a greater vulnerability to runaway breakdown associated with localized carrier injection.

One further process appears to contribute to the vulnerability of cells with metallized electrodes to RB-induced shunting: we have observed that the expulsion of a corrosive degradation product under RB-stress leads to dissolution and subsequent diffusion of metal electrodes into the perovskite layer. The

initial step (expulsion of a corrosive degradation product) will be discussed further below in reference to M4/D4. In figure 8, we show microscopic evidence of subsequent dissolution of the metal electrode (Fig 8c,d) and diffusion of electrode metal (in this case Ag) into the perovskite layer (Fig 8e,f). These process are likely to exacerbate hotspot formation relative to devices without metal electrodes, as metal ions within the perovskite layer are likely to increase its conductivity and/or the capacity for carrier injection at current-limiting interfaces.

Role of texture

Conceptually the effect of a non-planar texture on device behaviour (and in particular RB characteristics) be split into two categories: one, of effects arising from the influence of non-planar geometry on drift, diffusion and electrostatics (influence of sharp corners and valleys on ion accumulation and electric fields, for example), and the other concerning the effect of the texture on the formation and crystallization of the perovskite layer, as well as the cell's contact and electrode layers. The latter effects, having to do with a texture's impact on thin-film growth and crystallization, are evidently significant based on our microstructural characterization of devices made on textured Si (Fig. 7). In particular, perovskites grown on textured substrates via the hybrid method are especially prone to harbouring excess PbI_2 in the texture valleys, since the thermally evaporated PbI_2(+CsBr) templates are typically thicker in these regions. Our tests on flat devices have revealed the key importance of stoichiometry (under- and over-conversion) with respect to behaviour under reverse bias. These effects are expected to carry over to textured devices where under- and over-conversion are systematic issues associated with the hybrid method.

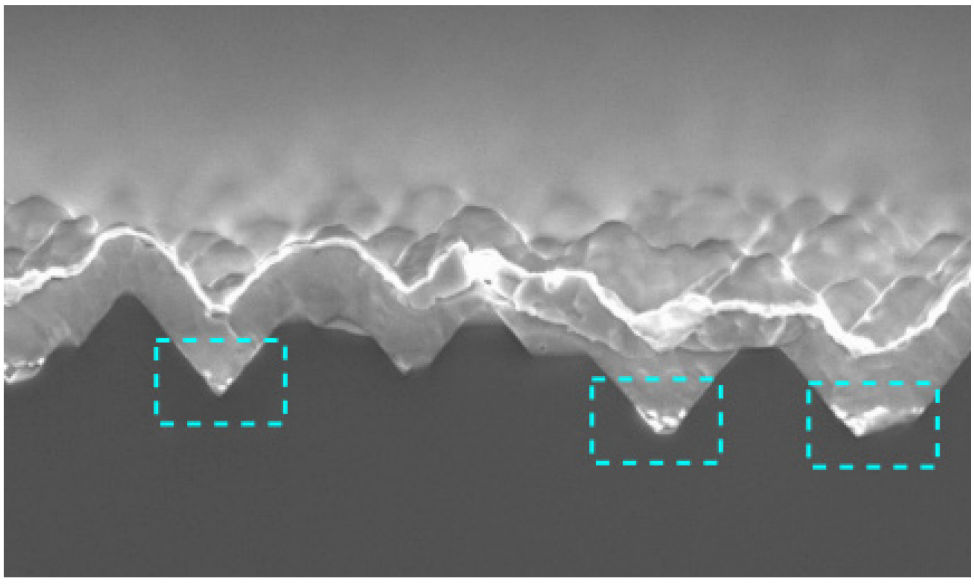

Figure 7: SEM cross-sectional view of a perovskite single-junction device on textured Si. Highlighted regions in the valleys show the presence of unconverted PbI_2 (a left-over from the template used in hybrid deposition), demonstrating a pronounced effect of the texture on local stoichiometry.

We did not attempt tests specifically aimed at investigating the intrinsic effects of texturing on e.g. internal fields due to the difficulty in seperating these from the fabrication effects mentioned above.

Role of polarity (n-i-p versus p-i-n)

Since the p-i-n polarity is relatively favourable for tandem integration we dedicated the bulk of our efforts to understanding and optimizing p-i-n cells, performing only preliminary investigations into the breakdown perovskite solar cells with the opposite (n-i-p) polarity. However, early tests indicate a number of commonalities between the two cases. In particular, reverse-bias was found to induce hotspots and localized breakdown in n-i-p solar cells, in a manner strongly resembling the behaviour

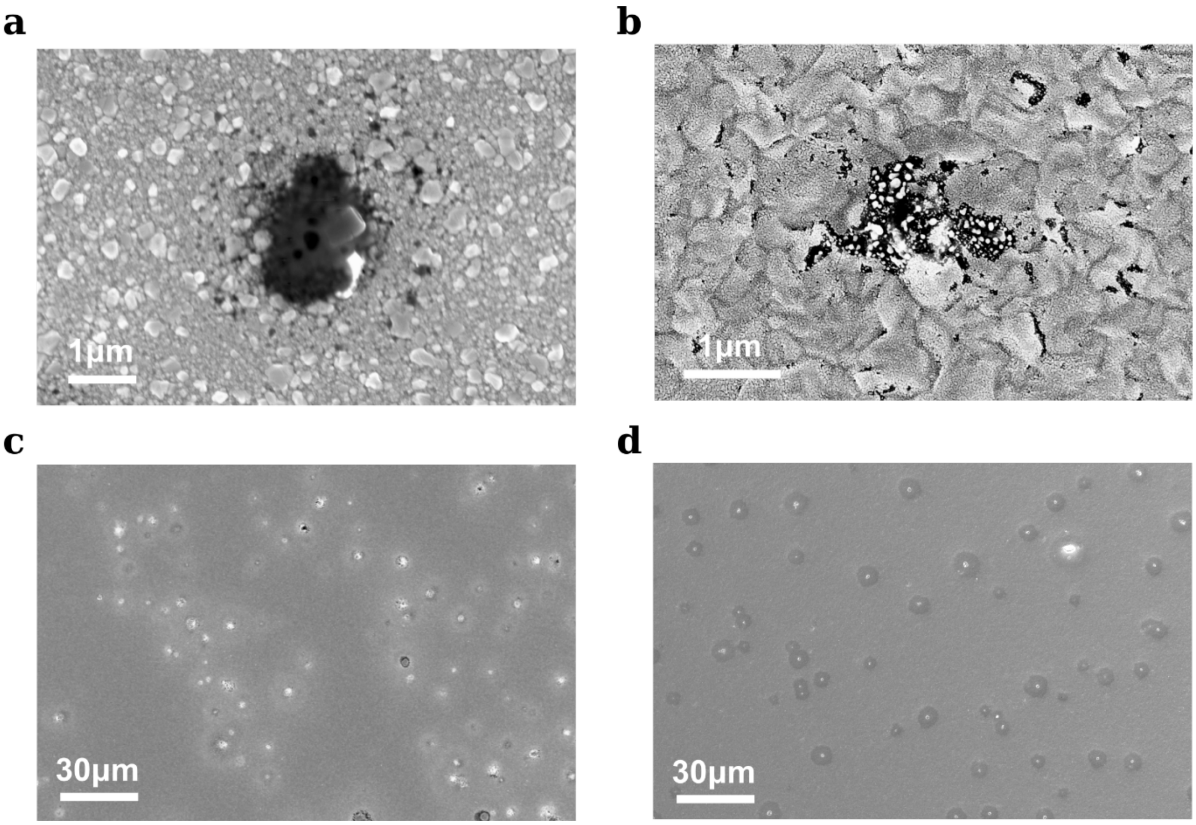

Figure 8: SEM top-view micrographs showing signs of RB-induced degradation in n-i-p (a,c) and p-i-n (b,d) solar cells. In both cases localized emission of a degradation product onto the top electrode surface (Au for the n-i-p, thin-Ag for the p-i-n in (b) and a normal-thickness Ag electrode in (d).

seen in our p-i-n devices. Figure 9 shows a comparison of the two cases, in which it can be seen that RB-stress leads to localized emission of a degradation product in devices with both polarities.

Despite the observation of localized current flow under RB in n-i-p devices and the appearance of hot-spot damage, this polarity seems to be less prone to actual shunt formation (meaning a localized ohmic current path that persists after the removal of RB). This may be a result of the thick HTL layer separating the perovskite and metal electrode in n-i-p cells (~200nm Spiro-OMeTAD compared to 20nm C_{60} in p-i-n architectures), which reduces the ability for metal from the top electrode to diffuse into the perovskite in high concentration. These early tests did not conclusively establish whether the degradation product seen in Fig 9a is corrosive with respect to Au electrodes in the same way that it affects Ag (Fig 6).

D3 - *J-V* curves (both forward and reverse conditions) as a function of temperature, illumination, pre-conditioning (forward or reverse bias, with or a without current flowing through the cell) of the cells defined in M2. Based on this data, definition of a protocol to assess tandems in reverse bias in field-relevant conditions (as illumination and operating conditions are different than for single junction devices).

The approach towards defining a standardized protocol for testing RB stability in tandems was reconsidered relative to our proposal for the sake of generality: rather than basing a suggested protocol on the behaviour of specific devices, we considered testing procedures that would better emulate partial-shading conditions in the field. Compared to single-junction photovoltaic devices, tandems are sensitive to the balance of current generation in the top versus bottom sub-cells, i.e. on the incident spectrum.

This is especially true in reverse-bias testing wherein the division of voltage is decided by current-matching. An excess of current generation in one or the other cell can entirely shift the applied reverse voltage from one cell to the other.

Using external quantum efficiency measurements obtained on the textured tandems generated by WPG1, and standardized spectra, we calculated that an excess of more than 1 mA cm^{-2} will be generated in a tandem top-cell under conditions where only the direct component of solar radiation is occluded (i.e. the sky remains visible from the vantage point of the cell, but not the sun itself). This implies that the Si bottom cell will generically sustain the entirety of any applied reverse voltage until its breakdown voltage is reached, as illustrated in Fig. 6ii.

Ideally, RB testing of tandems should be carried out under standardized conditions corresponding to the spectrum of diffuse solar radiation that would be encountered by a partially-shaded solar cell. In practice, since the current matching condition is decided merely the balance of currents, an adequate compromise would be to tune the spectrum used for testing to produce a current mismatch equal to approximately 1.4mA cm^{-2}, or the equivalent value calculated using the given cell's EQE. Most solar simulators have at least two degrees of freedom for tuning the output spectrum (e.g LED or lamp

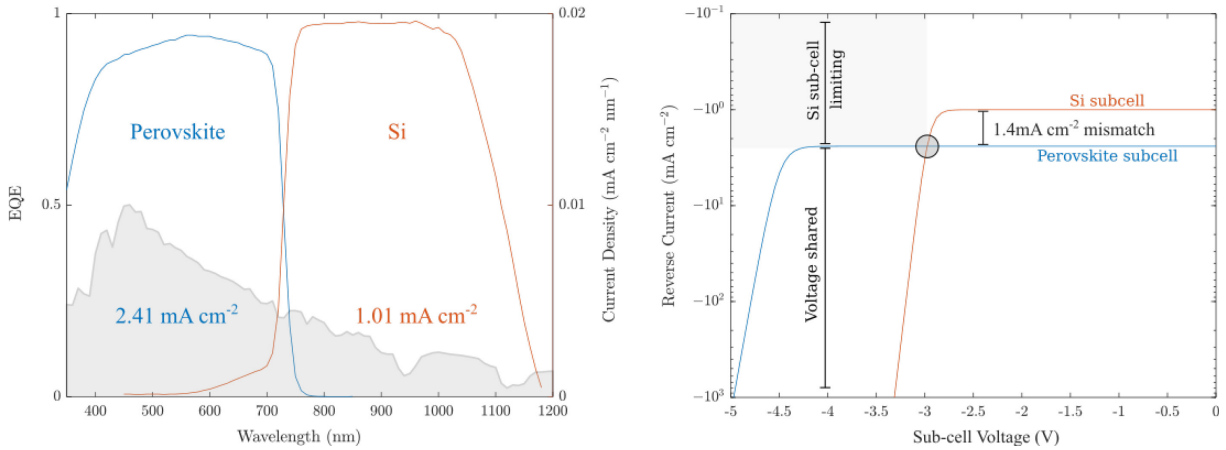

Figure 9: (Left) EQE of a high efficiency, fully-textured perovskite tandem shown with the spectrum of diffuse ("sky") radiation calculated using an air mass of 1.5. The excess of current in the perovskite top cell (corresponding to the blueness of the sky), implies that the Si bottom cell will be current-limiting under most partial-shading conditions. (Right) Schematic J-V curves for the Si and perovskite sub-cells of a tandem showing the effect of a blue-biased current-mismatch: the effect is to ensure that the Si cell is limiting for reverse currents up to its breakdown voltage (here approx. -3V), which would translate to approx. -6V on the cell (sum of sub-cell voltages).

currents) which would allow testing to be conducted under approximate partial-shading conditions. Below we describe a rough but flexible protocol for achieving this with an appropriate solar simulator.

Let the simulator's output be described by two variables x_B, x_R in the interval $[0,1]$, representing the intensity of the blue and red component respectively (these could represent the current in individual LEDs or lamp filaments, or variables representing a composite of several sources). The output is assumed to be linear in the control variables. It is not necessary however for the blue output to lie completely in the top-cell's absorption range, nor for the red to lie entirely in the bottom cell's (i.e. some overlap is tolerable), although clearly there must be sufficient differentiation to allow a mismatch of 1.4mA cm^{-2} to be generated. The currents in the top and bottom cells can then be written as

$$j_{sc}^{top} = j_B^{top} x_B + j_R^{top} x_R$$

$$j_{sc}^{bot} = j_B^{bot} x_B + j_R^{bot} x_R$$

with the current coefficients $j_{R,B}^{top,bot}$ describing the absorption of the blue and red light in the top and bottom sub-cells individually. Due to current-matching the tandem's current (measured at 0V) will be approximately

$$j_{sc}^{tandem} = \min[j_{sc}^{top}, j_{sc}^{bot}]$$

A protocol for setting the spectrum is then as follows.

1. Setting x_R to 1 (maximum), measure j_{sc}^{tandem} for at least two settings of x_B near 0 to determine j_B^{top}. Setting x_B to 0, measure j_{sc}^{tandem} for two settings of x_R near 1 to determine j_R^{top}.
2. Perform the converse procedure by setting x_B to 1 (maximum), and measuring j_{sc}^{tandem} for at least two settings of x_R near 0 to determine j_R^{bot}. Setting x_R to 0, measure j_{sc}^{tandem} for two settings of x_R near 1 to determine j_R^{top}.
3. Solve the simultaneous equations above with the determined coefficients to set conditions approximating a partial-shade spectrum, i.e.:

$$j_{sc}^{top} \equiv 2.41 \text{ mA cm}^{-2}$$

$$j_{sc}^{bot} \equiv 1.01 \text{ mA cm}^{-2}$$

This procedure was followed to perform the reverse-testing of tandems reported in Fig. 14 below.

Egress, not Ingress

An early hypothesis for RB degradation invoked metal migration from the top electrode, induced by the applied potential and occurring analogously to the process of electro-plating. This is the accepted operating principle of so-called electrochemical metallization memory devices,[2] and seemed to fit our

M4 - Identification of the atomistic mechanisms governing reverse bias stability of state of-the-art tandem solar cells.
D4 - Microstructural evidence (e.g. electron microscopy images, EDX spectra, lock-in thermography images and/or c-AFM maps) capturing how single-junctions and tandems degrade depending on reverse bias conditions (temperature, *J-V* conditions, illumination).

early observations of preferential breakdown around metallized portions of the active area (as compared with active area covered by only the TCO). However, many subsequent observations were made concerning RB failure that were either incompatible or unexplained by this hypothesis. Some of the observations in question were discussed above in the section on electrodes, and include the finding of RB shunt formation devices free of metal electrodes. Further indications as to the nature of RB breakdown were found by studying the degradation of so-called "thin-electrode" devices, in which a top-electrode of thin metal (approx. 15nm of silver) was used instead of a full-thickness layer (usually >100nm). This had the effect of exposing the top surface for characterization via surface-sensitive techniques, and reduced the detrimental effect of shunt formation (such hotspots would typically "burn out" quickly with the thin electrode, rather than compromising the entire device).

In Fig. 10 we show results obtained from the characterization of degraded thin-electrode devices (single-junction p-i-n devices on ITO-glass). Reverse-bias (here -4V for a duration of 30s) is seen to result in the expulsion of a degradation product onto the cell's top surface, dark in SEM contrast suggesting a light-element/organic composition. SEM Auger Spectroscopy (Fig. 10(b)) was used to determine that the degradation product enriches the top surface in iodine and nitrogen, the latter of which is likely to originate from the organic cation (the only nitrogen containing species in our perovskites). The

degradation product is highly corrosive with respect to the metal electrode where it emerges: this can be clearly seen in Fig 10d (also Fig. 8a) where the affected metal on the top surface appears in the form of a small droplets. In top-view SEM these droplets are typically surrounded by the dark degradation product.

Subsequent to being dissolved by the degradation product, metal from the top electrode can be found within the perovskite bulk. This was established by performing TEM EDX on thin lamellae cut from reverse-biased thin-electrode devices (Fig 8, a-d). The reactivity of the degradation product with respect to Ag is not particular to that metal: devices made with Au electrodes also degraded in a similar fashion (emission of a degradation product and local dissolution of the top electrode).

Of all the possible perovskite degradation products containing nitrogen and iodine, only one has been reported in the literature that possesses sufficient reactivity to dissolve metals including silver and gold: these are the organic polyiodide species such as MAI_x and FAI_x (x>2) that have been dubbed “reactive polyiodide melts”.[3–5] As a degradation product, these polyiodide melts are reported to emerge under illumination, either in long-term light-soaking or under intense laser-beam irradiation. We confirmed that our thin-electrode samples degraded under a laser-beam for a short duration showed very similar characteristics to those degraded under reverse bias. The schematic below summarizes the process by which RB damage seems to occur in our p-i-n devices.

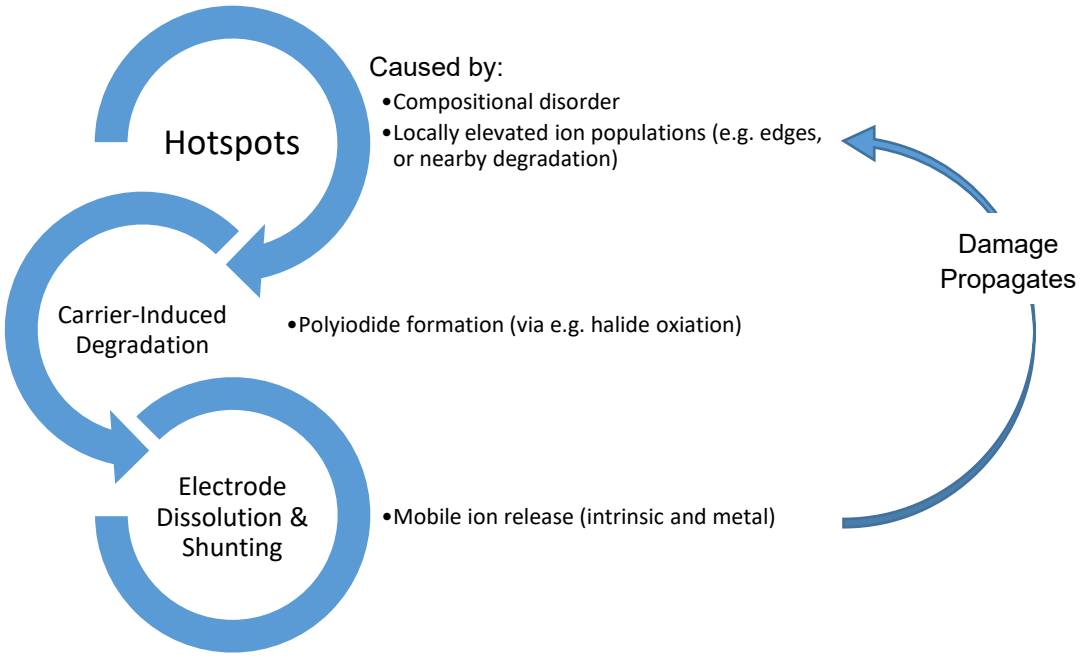

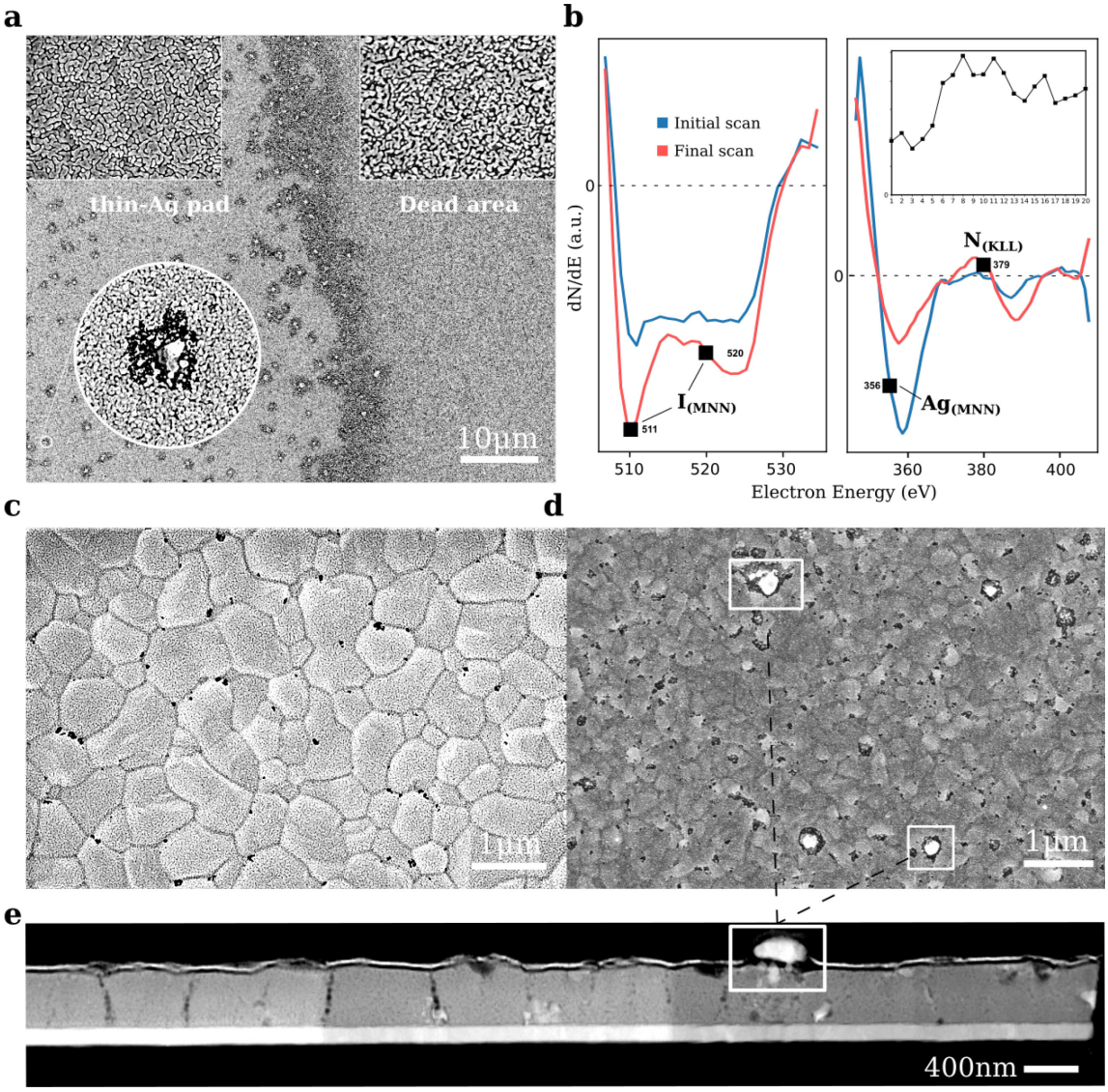

Figure 10: (a) SEM micrograph showing reverse-bias damage on a single-junction thin-electrode cell. Damage takes the form of a degradation product emitted onto the top surface (dark in SEM contrast), appearing in this sample with a pronounced concentration on the active area boundary (c.f. section below). (b) SEM Auger spectrum showing that the degradation product is rich in both iodine and nitrogen. (c) Lightly damaged cell showing a preference for emission at grain boundaries and intersections. (d) A more heavily degraded film (-4V 30s) showing islands of dissolved Ag electrode, also visible in the TEM cross-section shown in (e).

Lateral ion migration: degradation at edges

One of the most surprising and important outcomes of our mechanistic investigation into RB failure concerns the importance of cell boundaries. Like many dependencies discussed above, this fact was initially obscured by the effect of particle contamination, but even in early measurements a tendency for

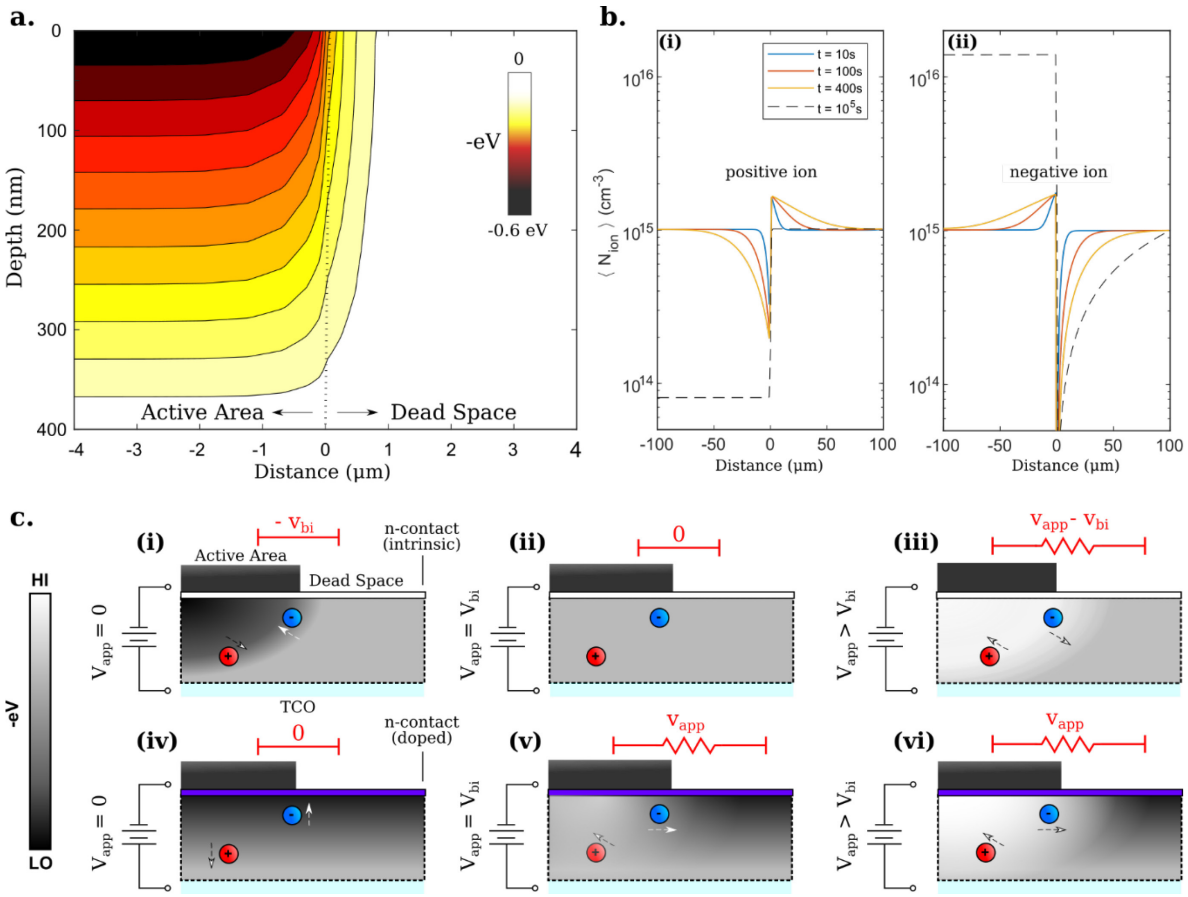

Figure 11 (a) Potential surface of a simulated p-i-n ITO/Monolayer/Perovskite/C_{60}/Ag stack cutting across the edge of the active area, versus depth from the top (Ag-side) surface. Shown is the internal potential inside the absorber layer only (potential dropped within the C_{60} layer is not shown). (b) Simulated density of mobile anions as a function of time, starting from initially homogenous distribution, under the action of the internal potential in (a). Densities are averaged across the film thickness. Equilibrium concentrations (reached after approximately 10^5s) are shown with a dashed line. (c) Qualitative schematics of the internal potential looking across an active area boundary for an intrinsic absorber in p-i-n configuration. The lateral potential difference across this boundary (red) depends on the doping level of the top selective contact (intrinsic in (i-iii), heavily doped in (iv-vi)), and on the applied voltage (symbol V_{app} in the figures). Lower-case letters are used to denote potential differences measured at the top surface of the absorber layer.

cells to degrade preferentially around their boundaries was frequently visible. Examples of edge-degradation under reverse-bias were shown already in Figure 5(d) and Figure 10(a).

Ion migration in perovskite devices is a well-accepted consequence of the halide perovskites' dual nature as high-performance semiconductors and fast ion conductors. The most significant form of ion migration for solar cells and other devices occurs across the film thickness as ions move in response to applied potentials, causing transient effects such as I-V hysteresis and charging currents. Our observations of RB failure around cell boundaries highlights the importance of considering *lateral* ion migration in addition to this more familiar mechanism, i.e. the redistribution of charged intrinsic species (vacancies and/or interstitials) across cell boundaries. The reasons for this lateral migration are identical: ions are driven by differences in the internal potential, in this case caused by discontinuities in the built-in or applied potential across substrate boundaries (e.g. ITO-edge or the boundary of metallization).

Since lateral ion migration across device boundaries is a logical consequence of the accepted theory describing mobile defects in perovskite (and other) materials, certain features could be explored using drift-diffusion calculations. In Fig 11a we show a drift-diffusion calculation of the internal potential across the edge of an active area, defined by the presence of metallization on the top surface of the simulated device. Parameters for these calculations were chosen to emulate our baseline p-i-n layer stack ITO/MeO-2PACz/Perovskite/C_{60}/Ag.

To demonstrate the manner in which lateral potentials drive a redistribution of anions and cations across active area boundaries, we incorporated charged drift-diffusing species into the simulation of Figure 11a to emulate both positive and negative ions. Using a 200um domain, 100um either side of a metallization boundary, we show in Figure 11b the concentration of this ionic charge as a function of time after initialization. Ions were initialized as a uniform concentration of uncompensated charges (1e15cm^{-3}), placed on both sides of the metallization edge, with blocking boundary conditions at the far limit of the active area, and a fixed concentration (equal to the initial 1e15cm^{-3}) at the far limit of the dead area. This latter choice emulates a situation in which the dead area acts as a limitless ionic source, approximating the physical case of either having a very small active area compared to the dead area on the substrate, or more loosely a situation in which ions are generated within the perovskite over time (e.g. through Frenkel-pair formation). The ionic diffusion constant was set to $D=10^{-8}cm^2s^{-1}$ to model the fastest moving species commonly measured in hysteresis and other transient techniques, usually attributed to halide defects. Given these assumptions, we find that the effect of the built-in potential is to drive a migration of negative ions into the active area resulting in concentration spikes near the active area boundary at short-to-intermediate times (Fig. 11b green and blue curves), and significant redistribution across the boundary as the simulation progresses. Once steady state is finally reached (dashed black in Fig 11b), taking as long as 10^5s with an ionic diffusion constant $D=10^{-8}cm^2s^{-1}$, ion concentrations in the active area - averaged over the film thickness - are approximately 20 times higher than their initial value for the anions, and 10 times lower for the cations, i.e. higher or lower than their value would remain in the absence of lateral migration from the dead space. This difference is driven by the built-in field alone: the application of forward or reverse bias will modulate the effect in a generally predictable way, taking proper account of the contact-layer and absorber doping (Fig 11c – a detailed discussion of these schematics will be omitted in this report, to appear in a future publication).

Lateral migration at cell boundaries leads to enhanced ion concentrations in those locations, and as a result in higher local current densities under RB-stress. Fig 12a shows an example of a cell passing a higher reverse current along its active-area boundary (in this sequence the pattern degenerates into hotspots after several repeated tests). Microscopic investigation of these cells shows that these edges suffer much worse material degradation than the surrounding active area, as can be seen in Fig. 10a. Observations of cells under RB-stress in photoluminescence (Fig 12b,c,d) provide useful information on the identity of the laterally diffusing ion, from its charge to allowing estimates of a diffusion constant (Fig 12d). Details of these measurements will be deferred to a forthcoming publication. However it is worth noting here that over several experiments on a range of devices it has become clear that more than one ionic species is likely to be active in lateral migration. This can be inferred from patterns of degradation, which point to positively charged species in some experiments and negatively charged ions in others, and from the direct observation of e.g. lateral diffusion of metal ions, which is at least one species able to produce effects such as those shown here (but certainly not the only one, as even metal-free cells are subject to these phenomena).

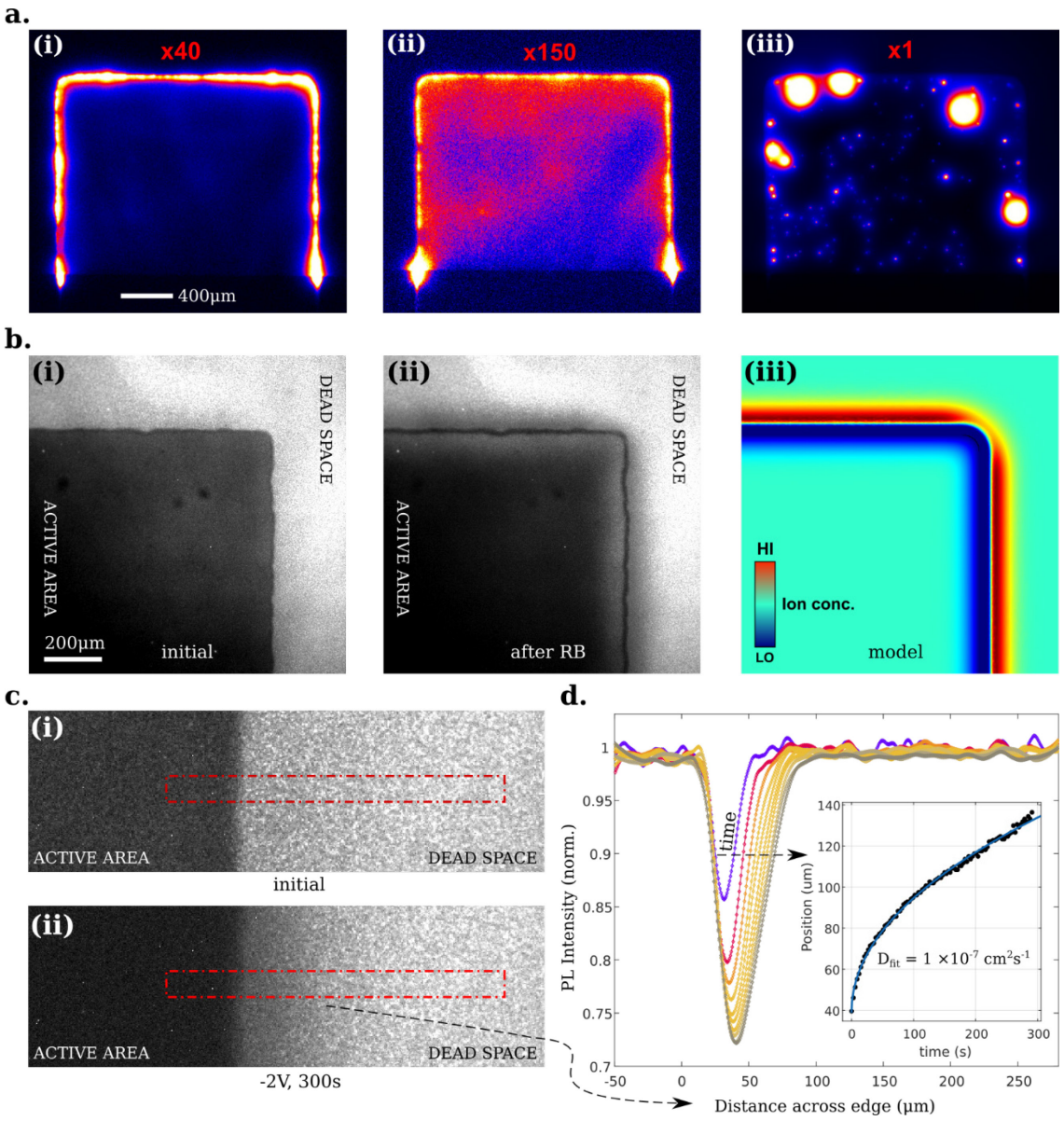

Figure 12 (a, i-iii) Sequence of lock-in thermography images acquired at -4V (25Hz), approximately 60s per acquisition, showing current concentration along the active area boundary in (i), tending to a more uniform distribution in the second acquisition (ii), and finally degenerating to a collection of hotspots in (iii). Red labels indicate scaling of the amplitude images relative to (iii). (b) Photoluminescence images showing the corner of an active area (thin-electrode) before (i) and after (ii) a reverse-bias test conducted at -4V under N_2 atmosphere. In (iii) we show a simulation of positive ion migration under reverse-bias which mimics the geometrical features visible in (ii). (c) Close-ups of the experiment in (b) showing darkening around the cell boundary that spreads outwards as a function of time. (d) Plots of the PL intensity at the boundary averaged within the red rectangle shown in (c) – values were normalized to the initial condition shown in (i).

3 Optimisation of cell architecture for an enhanced long-term stability (Work-package 3)

The purpose of INTENT's final work-package was to implement the understanding gained from work-package 2 to drive the optimization of more resilient Si/perovskite tandems.

M5 – Demonstration of perovskite/silicon tandem cells passing IEC tests and exhibiting an improved reverse bias resistance.
D5 - *J-V* curves of optimised tandem devices (initial efficiency at maximum power point >26% for a 1 cm^2 device), which show limited degradation for various 0 and 0.5 sun illumination conditions (minimum requirement of <5% after one hour at -1.5V) and pass IEC standard tests (damp heat, thermal cycling, light soaking tests).

It is well-known that the challenge of making stable perovskite devices hinges on proper encapsulation in the broadest sense: meaning not only device layers that isolate the perovskite from the environment (humidity & oxygen in particular), but which also restrain the perovskite components from inter-diffusing and reacting with adjacent layers (e.g. metal electrode). In work-package 2 we discovered that reverse-bias degradation proceeds via the emission of a corrosive degradation product whose subsequent reaction with metal electrodes causes catastrophic shunting. To prevent this degradation path, and perhaps supress the emission of degradation products altogether, we invested considerable effort into optimizing our ALD SnO_x buffer layers. These layers play an initial role of protecting the underlying perovskite during the sputtering process used for making transparent top electrodes, but also play a key role in subsequent stability.

Figure 13a shows that without careful attention the SnO_x layers grown on our perovskite device layers are not guaranteed to be dense and conformal, as is frequently assumed for ALD-type growth. A number of trials were conducted to optimize the deposition parameters (pulse widths, flow rates, purge times, temperature and number of cycles) to obtain dense SnO_x layers that would act as better barriers, ensuring long-term stability. Fig. 13b shows the obtained morphology for our optimized layers with the insets showing enhanced stability to moisture in a water-droplet test.

With improved ALD buffer layers, and the lessons learned from work-package 2 regarding contamination, we were able to significantly improve the RB-stability of our baseline devices. This is shown in Fig. 14a, where we compare the RB-behaviour of a recently-made, clean device with that of typical devices taken from more than five separate experiments conducted early in the project. The data shows the cell's shunt resistance, whose evolution can indicate the occurrence of RB-induced shunting as discussed earlier in this report – in this figure shunting is indicated by a sudden decrease in the shunt resistance, whereas the gradual droop seen in our recent devices corresponds instead to reversible changes associated with ion accumulation.

Experiments conducted early in INTENT's timeline often yielded devices that would shunt catastrophically at voltages as low as -0.5V, and after only a few seconds (Fig. 14b). Improvements to cleanliness and the quality of our buffer layers made during the course of the project have finally yielded devices which survive up to -1.5V for 1 hour, and possibly much longer, without shunting (Fig. 14c), and without losing any efficiency after a recovery period. Although these devices were single-junction solar cells, this test represents a much tougher obstacle for the perovskite sub-cell than would testing in a full tandem, due to the projective effect of the Si bottom-cell. We therefore regard these results as sufficient to show that Si/perovskite tandems can be made to pass the D5 goal of less than 5% performance loss after biasing at -1.5V for 1 hr. These devices still undergo reversible a performance loss associated with ion migration however,[6] which is notably found to be worst at the active area boundaries (Fig. 14b). These boundaries therefore appear to be the bottleneck at present with respect to further improving the RB-stability, and ideally mitigating the reversible performance loss, which can take up to several hours to recover (Fig 14c inset).

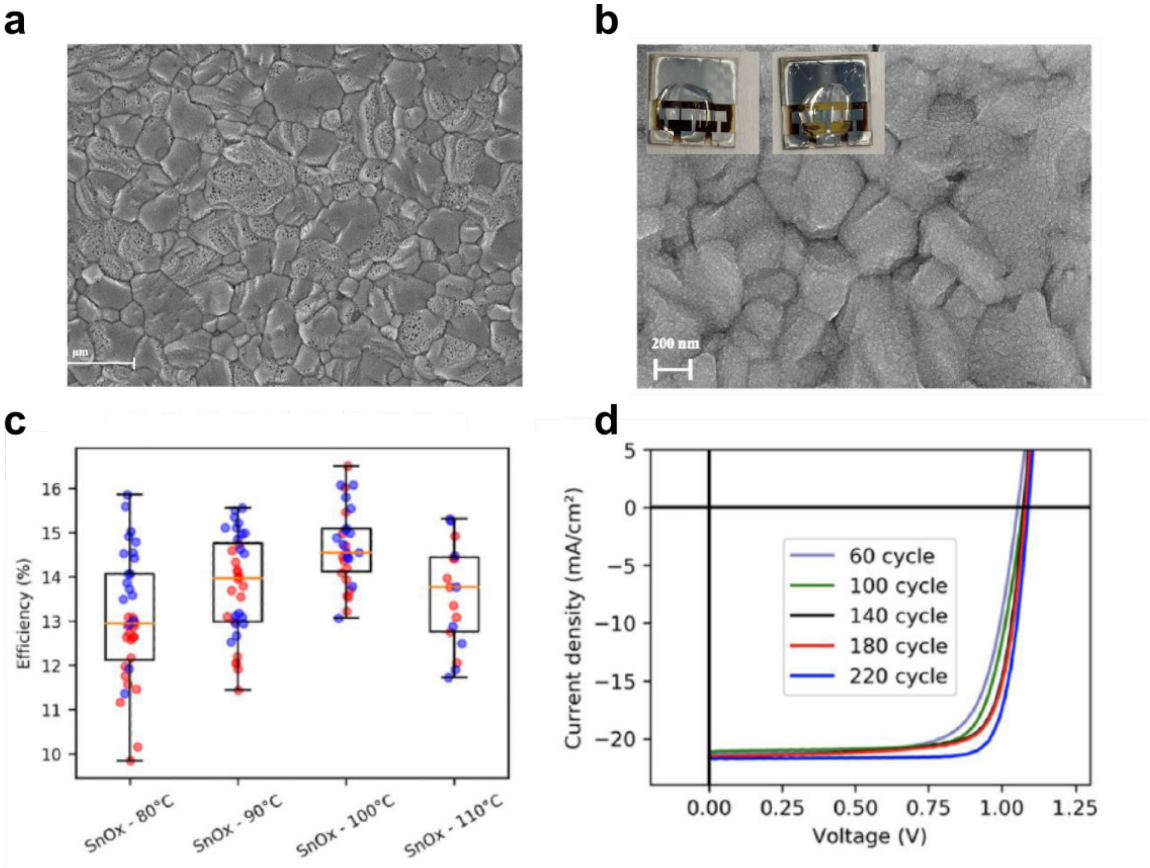

Figure 13: Optimization of the ALD SnOx buffer layer. (a) Porous morphology seen in some ALD SnO_x layers prior to optimization. (b) Compact morphology obtained after optimization. Insets show photographs of cells with compact SnO_x on the left and porous SnO_x on the right after exposure to a water drop for 15min. (c) Device performance as a function of the SnO_x deposition temperature (single-junction cells prepared via the one-step method) and thickness or number of cycles (d).

Tests were also conducted on the stability of our baseline tandem devices – one of which is shown in Fig. 14d. Here we conducted a blue-biased reverse-stability test (following the protocol outlined above with respect to D3) and found a minimal performance losses, as would be expected for an intact bottom cell (which should effectively shield the top-cell from reverse voltage).

To test the limits of reverse-stability in our champion devices, a select few were biased at reverse voltages up to -7V. As shown in Fig 14e, these test-cells (made with our optimized buffer and thin-Ag electrodes) were able to pass reverse-currents of more than 50 mA cm^{-2} without showing any of the typical signs of RB-degradation discussed above in devices without a SnOx buffer (Fig 10 – note that those tests were conducted at only -4V).

Due to the late delivery of stability-testing equipment from a supplier (light-soaker with climatic chamber for long-term MPP stress-tests), which is still being assembled at the time of this writing (more than 1 year late according to our purchase plan), we were unable to perform extensive stability tests on our optimized single-junction and tandem devices. Partly as a result of this delay we shifted the bulk of our efforts in INTENT towards work-package 2, a shift that was also motivated by the complexity of phenomena associated with RB degradation, which are still being fully elucidated.

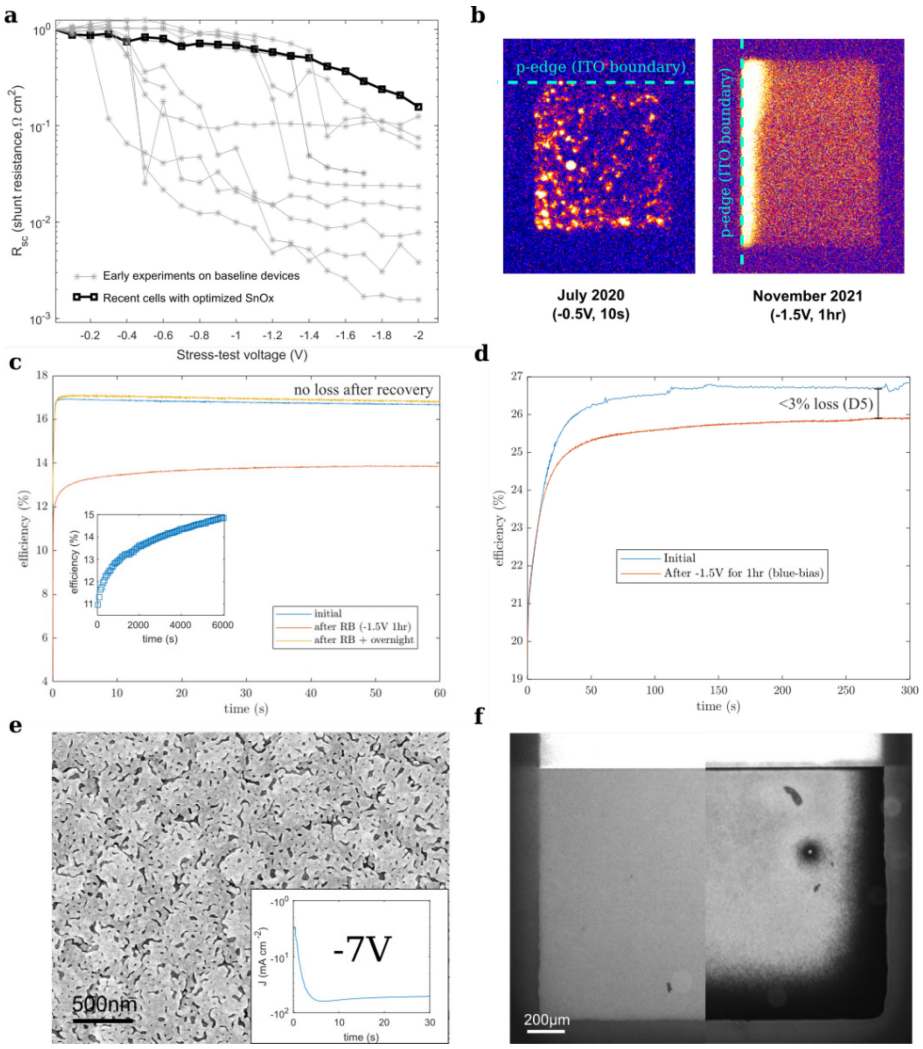

Figure 14: (a) Progress in avoiding the early shunting associated with particle contamination. Recent devices suffer reversible performance losses but do not suffer from the sudden development of shunts, as was seen very frequently in early experiments. (b) Heat maps showing severe hotspot formation in early devices (left) even after extremely mild RB exposure, as compared with recent cells made using our optimized SnOx layer (right), which last for much longer at more extreme voltages without suffering from hotspot formation (although edges remain a bottleneck). (c) A test conducted for the D5 deliverable showing MPP efficiency of a single-junction hybrid cell (all fabrication processes fully compatible with tandem production) before and after RB-stressing at -1.5V for 1hr. The cell was found to suffer an initial performance drop which recovered on the time-scale of several hours (inset). The efficiency measured after 12 hours showed no loss with respect to the initial measurement. (d) Measurement of tandem efficiency conducted under blue-light bias as described in this report. A small loss in performance of 3% after testing can likely be attributed to handling damage. (e) SEM micrograph showing a thin-electrode cell with our optimized SnOx buffer after exposure to -7V for 30s. Surprisingly, no signs of damage are visible on the cell's top surface, despite the device passing a reverse-current density of more than 50 mAcm^{-2}. (f) Photoluminescence images taken before (left) and after (right) a reverse-bias test on an identical device to the one shown in (c), demonstrating the importance of edge effects (lateral ion migration) as a bottle-neck in RB stability for this cell type.

D6 - Report on the implementation of the optimised tandem cell design in current monocrystalline Si SHJ process lines.

Based on the findings of our mechanistic investigation (WP2) we have identified three factors of high importance regarding the RB-stability of perovskite cells. These are

1. The problem of particle contamination.
2. The importance of cell boundaries and dead space.
3. The significance of compositional homogeneity.

These points relate most straightforwardly to single-junction perovskite cells and all-perovskite multi-junctions, wherein the perovskite cell must ultimately either pass reverse current without degrading, or

at least sustain reverse voltage without significant performance loss. In Si/perovskite tandems the bottom-cell will generally be current limiting under conditions of partial-shade as discussed in the D3 section above, and this implies that the reverse voltage will drop, up to a fairly large threshold, entirely within the Si device. As Si cells are comparatively stable this fact naturally renders tandems much more resilient than all-perovskite devices under the threat of partial-shading. To clarify the extent of this resilience future studies would need to identify the probability of encountering red-biased spectra (e.g. perhaps induced by a dust-storm or highly polluted skies) under real-world conditions. Accordingly, tandem devices could be fabricated with an intentional current mismatch favouring the top-cell (i.e. bottom-limited conditions under the AM1.5G spectrum) to provide an extra margin of safety in case the cell encounters partial-shade spectra with a red-light bias. These modifications can be trivially executed by adjusting the thickness of the perovskite absorber. Any performance loss resulting from the intentional current-mismatch would have to be weighed against the risk of such unexpected partial-shading events, the native RB resilience of the perovskite top-cell, and the number of bypass diodes available in modules.

In the worst-case scenario for a tandem, the protective effect of the Si bottom cell is insufficient (this could either be due to an inadequate budget for bypass diodes, or atypical partial shading conditions). In this case all three points listed above come into play. We have seen in our studies that the presence of particle contamination can lead to complete device failure under RB at voltages much milder than the breakdown of the cell itself – particle-induced shunting is therefore likely to be the first point of failure. In our glovebox-based fabrication sequence, detrimental contamination is generated in large quantities by our metal evaporators and sputtering tools. Commercial production of tandem devices, if it ever becomes viable, will be conducted in clean-room environments exceeding the standards of most laboratories. However, the threat of contamination arising from neighbouring processes will remain, and potentially be worse due to high production volumes. Measures will have to be taken to ensure isolation of processing steps such that there is no back-flow of particles generated in, e.g. electrode deposition to the earlier stages of absorber fabrication. This may be an issue of special concern for production based on the use of cluster-tools, which combine several processing steps in close spatial proximity. Although the dire threat of contamination is equally understood by the research community and the industrial sector, tests would usually be conducted by examining solar cells in forward bias (i.e. measuring efficiency). Our experience shows that this is quite inadequate for establishing the RB-stability of perovskite devices, as many forms of contamination remain completely benign in forward-bias until activation after RB is applied.

The significance of lateral ion migration for Si/perovskite tandem devices is difficult to assess at present. Wafer-scale tandems will avoid the detrimental effects associated with having active area boundaries and dead-space, as the entire wafer is utilized (with the exception of metallized regions which remain active but shaded), by contrast with lab-scale devices. However lateral migration may manifest in a different way as a means by which local degradation spreads elsewhere in the wafer. Further work is ongoing to establish the connection between the modes of degradation uncovered in INTENT and other forms of instability, such as degradation under illumination or MPP tracking (operational instability).

We have shown that compositional inhomogeneity on a microscopic scale leads to hotspot formation and eventually shunting in perovskite devices that are forced to pass reverse current. Again, this can only be expected to occur in tandems under extreme conditions, but here tandems are likely to fare worse than their single-junction counterparts due to the extreme difficulty of ensuring compositional uniformity on the randomly textured surface of an industrial Si bottom-cell. Due to the severity of these issues already in single-junctions, the best strategy for protecting tandems may be to follow our approach of suppressing reverse-current injection (through the use of, e.g. thicker contacts or buffer layers), which will reduce the impact or likelihood of hotspot formation. Bypass diodes as ever are another viable solution.

The majority of the processes used to fabricate our most stable devices have scalable analogues that could conceivably be implemented into monocrystalline Si SHJ process lines. The most stable of our cells reported in Fig 14 were based on the hybrid method, that has been refined at PV-Lab over several years to deposit high-performing top-cells on Si cells with industry-standard textures. Our main innovation with respect to improving stability, being a dense and conformal SnO_x layer, was prepared by ALD, which is not a-priori an easily scalable process due to long processing times. However, spatial ALD could potentially solve this issue and has already been used to show comparable and even superior performance when used to prepare SnOx buffer layers in perovskite devices.[7]

References

1. Bowring, A. R., Bertoluzzi, L., O'Regan, B. C. & McGehee, M. D. Reverse Bias Behavior of Halide Perovskite Solar Cells. *Adv. Energy Mater.* **8**, 1702365 (2018).
2. Valov, I., Waser, R., Jameson, J. R. & Kozicki, M. N. Electrochemical metallization memories - Fundamentals, applications, prospects (Nanotechnology (2011) 22 (254003)). *Nanotechnology* **22**, (2011).
3. Shlenskaya, N. N., Belich, N. A., Grätzel, M., Goodilin, E. A. & Tarasov, A. B. Light-induced reactivity of gold and hybrid perovskite as a new possible degradation mechanism in perovskite solar cells. *J. Mater. Chem. A* **6**, 1780–1786 (2018).
4. Udalova, N. N. *et al.* New Features of Photochemical Decomposition of Hybrid Lead Halide Perovskites by Laser Irradiation. *ACS Appl. Mater. Interfaces* **12**, 12755–12762 (2020).
5. Petrov, A. A. *et al.* Methylammonium Polyiodides: Remarkable Phase Diversity of the Simplest and Low-Melting Alkylammonium Polyiodide System. *J. Phys. Chem. Lett.* **10**, 5776–5780 (2019).
6. Jacobs, D. A. *et al.* Hysteresis phenomena in perovskite solar cells: The many and varied effects of ionic accumulation. *Phys. Chem. Chem. Phys.* **19**, 3094–3103 (2017).
7. Hoffmann, L. *et al.* Spatial Atmospheric Pressure Atomic Layer Deposition of Tin Oxide as an Impermeable Electron Extraction Layer for Perovskite Solar Cells with Enhanced Thermal Stability. *ACS Appl. Mater. Interfaces* **10**, 6006–6013 (2018).